Semiconductors Hot Paper

How to cite: *Angew. Chem. Int. Ed.* **2023**, *62*, e202301191
International Edition: doi.org/10.1002/anie.202301191
German Edition: doi.org/10.1002/ange.202301191

$Sr(Ag_{1-x}Li_x)_2Se_2$ and $[Sr_3Se_2][(Ag_{1-x}Li_x)_2Se_2]$ Tunable Direct Band Gap Semiconductors

*Xiuquan Zhou, Brandon Wilfong, Xinglong Chen, Craig Laing, Indra R. Pandey, Ying-Pin Chen, Yu-Sheng Chen, Duck-Young Chung, and Mercouri G. Kanatzidis**

Abstract: Synthesizing solids in molten fluxes enables the rapid diffusion of soluble species at temperatures lower than in solid-state reactions, leading to crystal formation of kinetically stable compounds. In this study, we demonstrate the effectiveness of mixed hydroxide and halide fluxes in synthesizing complex Sr/Ag/Se in mixed LiOH/LiCl. We have accessed a series of two-dimensional $Sr(Ag_{1-x}Li_x)_2Se_2$ layered phases. With increased LiOH/LiCl ratio or reaction temperature, Li partially substituted Ag to form solid solutions of $Sr(Ag_{1-x}Li_x)_2Se_2$ with x up to 0.45. In addition, a new type of intergrowth compound $[Sr_3Se_2][(Ag_{1-x}Li_x)_2Se_2]$ was synthesized upon further reaction of $Sr(Ag_{1-x}Li_x)_2Se_2$ with SrSe. Both $Sr(Ag_{1-x}Li_x)_2Se_2$ and $[Sr_3Se_2][(Ag_{1-x}Li_x)_2Se_2]$ exhibit a direct band gap, which increases with increasing Li substitution (x). Therefore, the band gap of $Sr(Ag_{1-x}Li_x)_2Se_2$ can be precisely tuned via fine-tuning x that is controlled by only the flux ratio and temperature.

Introduction

Flux reactions use molten salts and are powerful tools for crystal growth and the discovery of new materials. Unlike the traditional solid-state reactions by direct stoichiometric combination of solids, fluxes dissolve reactants and intermediates and allow reactions at lower temperatures, enabling access to new reaction paths, leading to a greater number of phases.[1] Molten alkali hydroxides have been used successfully in synthesizing various metal oxides[1e,2] because the reactivity and solubility of metal cations can be tuned by the acid-base chemistry in molten hydroxides.[3] In addition, when hydroxides are mixed with water in a semi-closed system, they become a new type of flux, known as hydroflux, which is effective for hydroxide synthesis.[1d,4] Hydroflux can also be used for chalcogenides (Q) synthesis by in situ formation of Q^{2-} via the reduction of QO_2.[5] Interestingly, hydroxide fluxes alone have not been used as a reaction medium for chalcogenides prior to our work,[6] despite good solvents for both metal oxides[2] and alkali chalcogenides.[7] Our recent work on ternary K–Ni–S using mixed KOH/LiOH fluxes demonstrates mixed hydroxide/halide fluxes as promising candidates for exploratory chalcogenide synthesis. The mixed flux can stabilize all known ternaries of K–Ni–S, α-$K_2Ni_3S_4$, and KNi_2S_2 and novel metastable phases such as KNi_4S_2, $K_4Ni_9S_{11}$ and β-$K_2Ni_3S_4$.[6] In addition, we reported that phase selection is controlled by only two parameters: basicity (solubility) and sulfur concentration, regardless of the ratios of the other starting materials, allowing precise and facile product selection.[6] The flux system also enables the use of versatile and easily accessible precursors such as NiO, $Ni(OH)_2$, or $NiCl_2$ and elemental sulfur as Ni and S sources, respectively. Based on our recent findings with Ni and Cu chalcogenides,[6,8] the aforementioned features make mixed hydroxide fluxes promising reaction media for exploring novel chalcogenides.

In this study, we demonstrate effectiveness of hydroxide/halide fluxes as a medium for synthesizing $Sr(Ag_{1-x}Li_x)_2Se_2$ (x = 0–0.45) and $[Sr_3Se_2][(Ag_{1-x}Li_x)_2Se_2]$. We were also able to precisely control the extent of Li substitution (x) by tuning the LiOH/LiCl ratio using the mixed hydroxide/halide flux. LiOH is an effective solvent that ensures high solubility, whereas LiCl is an anti-solvent that modulates solubility. $SrAg_2Se_2$ is the first ternary chalcogenide in the Sr–Ag–Q family (Q = S, Se, Te). Silver chalcogenides have attracted significant attention over the past few years owing to their excellent thermoelectric properties[9] and super-ionic conduction in confined dimensions;[10] however, ternary systems with alkaline earth metals (AE) are scarcer than systems with alkali metals.[11] We were unable to form $SrAg_2Se_2$ using direct combination reactions. In general, direct-combination solid-state reactions do not work well with these systems. For example, $BaAg_2S_2$ has only been reported to be obtained by heating barium-bis[dicyanoargentate(I)] under H_2S gas flow[12] and $Ba_2Ag_8S_7$ has been prepared using an electrochemical method in a solution of ethylenediamine.[13] When $Ba_2Ag_8S_5$,[14] which is structurally similar to $Ba_2Ag_8S_7$ but without an S–S bond,

[*] X. Zhou, X. Chen, D.-Y. Chung, M. G. Kanatzidis
Materials Science Division, Argonne National Laboratory
9700 South Cass Avenue, Lemont, IL 60439 (USA)
E-mail: m-kanatzidis@northwestern.edu
B. Wilfong
United States Naval Academy
121 Blake Rd, Annapolis, MD 21402 (USA)
C. Laing, I. R. Pandey, M. G. Kanatzidis
Department of Chemistry, Northwestern University
Evanston, IL 60208 (USA)
Y.-P. Chen, Y.-S. Chen
NSF's ChemMatCARS, the University of Chicago
9700 South Cass Avenue, Argonne, IL 60439 (USA)

was targeted using the solid-state method by direct reaction of stoichiometric BaS, Ag, and S, the yield was less than 20 %, and significant amounts of binary impurities such as BaS, BaS_2, and BaS_3 were present. It is likely that trivial binaries are more thermodynamically favorable than ternary compositions and are difficult to bypass using traditional solid-state methods. Therefore, the hydroxide/halide flux method is not just an alternative for discovery synthesis methodology but a unique approach for many unique compounds. Our Density Functional Theory (DFT) calculations and spectroscopic measurements suggest they are direct band gap semiconductors with E_g as a function of x from 1.59 to 1.95 eV for $x=0$ to 0.38, respectively. These features make $Sr(Ag_{1-x}Li_x)_2Se_2$ an attractive candidate for photovoltaics or thermal neutron detection because the atomic percentage of Li can be as high as 18 %.[15]

Results and Discussion

The high solubility of oxides in molten hydroxide fluxes allows the use of simple precursors such as SrO or Ag_2O in synthesis reactions.[2] The dissociated cations can react with an anion such as a chalcogenide (Se^{2-}), which forms from the disproportionation of Se under very basic conditions, to form Ag–Se bonds. Remarkably, despite its extreme hydroxide basicity, this reaction medium does not interfere with the formation of metal chalcogenide bonds. For the Sr/Ag/Se system, a new ternary $SrAg_2Se_2$, isostructural to $BaAg_2S_2$ (*P*-3*m*, Table S1),[12] readily forms. To determine if this phase could be formed by the classical solid-state reaction, we attempted to synthesize $SrAg_2Se_2$ using SrSe with Ag_2Se (1:1 molar ratio) at 500 and 1000 °C. The synthesis was unsuccessful, yielding only unreacted precursors such as SrSe and Ag_2Se (Figure S1). No quaternary phase was formed either when we targeted $Sr(Ag_{0.8}Li_{0.2})_2Se_2$ using $SrSe:Ag_2Se:Li_2Se=1:0.8:0.2$, suggesting that the molten alkali hydroxide/alkali halide reaction medium in this study is unique in enabling the reaction path to $SrAg_2Se_2$.

Interestingly, the Ag atom site of the structure can be partially replaced with Li to form $Sr(Ag_{1-x}Li_x)_2Se_2$, where x is the extent of Li substitution with Ag. The generic reaction equation for this process is as follows:

$$Sr^{2+} + 2xLi^+ + 2(1-x)Ag^+ + 2Se^{2-} \rightarrow Sr(Ag_{1-x}Li_x)_2Se_2 \quad (1)$$

The value of x can be controlled by adjusting the LiOH fraction in the flux, r(LiOH), and the temperature (T). When r(LiOH) or T was increased, the value x in the product also increased, as demonstrated by the selected samples described in Table 1.

Low x values (<0.1) were obtained for reactions at 450 °C, as shown in Table 1. However, these products were often mixed with Ag_2Se impurities. For reactions with [OH] below 0.7 at 450 °C, the products were primarily Ag_2Se and unreacted SrO or SrSe. When the reaction temperature was increased to 500 °C or above, the formation of binary Ag_2Se was suppressed and pure products were obtained, as shown by the powder X-ray diffraction (PXRD) patterns in Figure 1b. At $T=500$ °C and [OH] <0.7, $Sr(Ag_{1-x}Li_x)_2Se_2$ with $x<0.16$ was still obtained, but the as-recovered products contained significant amounts of Ag_2Se. Therefore, to target $Sr(Ag_{1-x}Li_x)_2Se_2$ with low x, we conducted reactions at 600 °C with [OH] <0.7. For [OH] $=0.58$ at 600 °C, we obtained $SrAg_2Se_2$ ($x=0$) without Ag_2Se. Following a similar trend, x also increased with an increased [OH] at 600 °C.; however, when [OH] increased above 0.83, metallic Ag formed. It is likely that Ag^+ can be reduced to Ag^0 by Se^{2-} when the basicity is high enough, similar to our observations of reactions between Ni^{2+} and S^{2-} in mixed KOH/LiOH, in which high basicity results in metallic Ni.[6] These findings described above suggest that reactions in LiOH/LiCl fluxes exhibit solution-based reaction characteristics, such as pH-dependent oxidation states in aqueous solutions.[17]

We conducted differential thermal analysis (DTA) to study the stability of $Sr(Ag_{1-x}Li_x)_2Se_2$ and explain why direct combination reactions were unsuccessful. The first heating cycle for $SrAg_2Se_2$ (sample 1, $x=0$) (Table 1) showed an anomaly during cooling around 580 °C, suggesting an endothermic event (Figure S2a), whereas no such features were observed during subsequent cycles (2–3) (Figure S2b). Similarly, inconsistency between the first and subsequent

Table 1: Synthetic conditions and lattice parameters for $Sr(Ag_{1-x}Li_x)_2Se_2$. The extent of Li substitution (x) increases with increasing r(LiOH) (defined as $r(\text{LiOH})=n(\text{LiOH})/[n(\text{LiOH})+n(\text{LiCl})]$) or T. LiCl is used to modulate the basicity and solubility of the flux, which is crucial for tuning x. The crystallographic data are described in Table S1–8.[16] The single crystal X-ray diffraction (SXRD) data for Samples 1 and 6 marked with "*" were collected using a synchrotron X-ray source with a wavelength $\lambda=0.41328$ Å, whereas the rest of the samples were collected using laboratory X-ray sources. In addition, comparison between lab X-ray and synchrotron data were collected for sample 5 and 8, which are shown in Table S10 and S11, respectively. $Sr(Ag_{1-x}Li_x)_2Se_2$ crystallize in the *P*-3*m* space group.

Sample	r(LiOH)	T [°C]	a [Å]	c [Å]	V [Å^3]	Li
1*	0.57	600	4.4096(2)	7.1966(4)	121.187(13)	0
2	0.73	450	4.4260(3)	7.2176(5)	122.446(19)	0.077(6)
3	0.80	450	4.4188(3)	7.2109(6)	121.935(19)	0.098(6)
4	0.73	500	4.4119(4)	7.2041(7)	121.44(2)	0.166(4)
5	0.76	500	4.4074(2)	7.204(5)	121.191(14)	0.255(4)
6*	0.80	500	4.4076(1)	7.2147(3)	121.382(7)	0.337(3)
7	0.83	500	4.3973(6)	7.1800(14)	120.23(4)	0.381(8)
8	0.86	550	4.3885(12)	7.188(2)	119.88(7)	0.438(6)

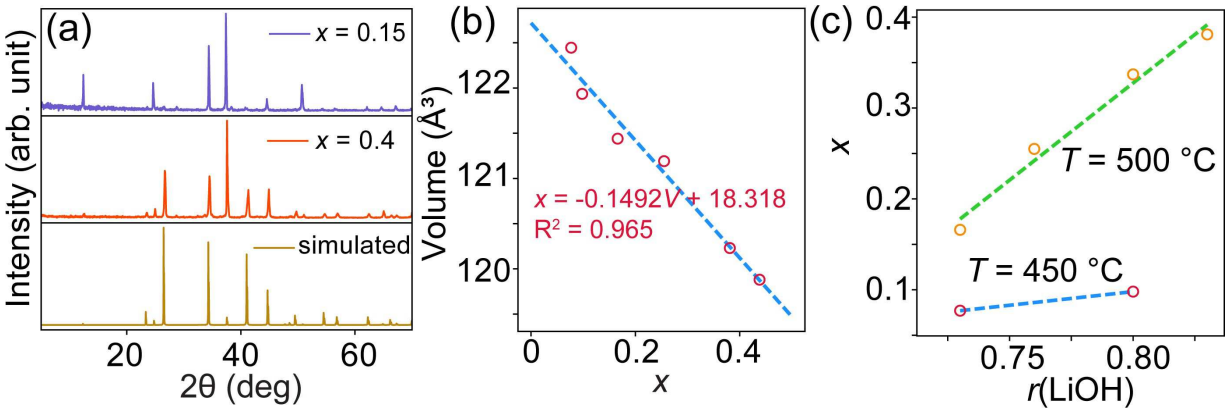

Figure 1. Powder X-ray diffraction (PXRD) results for $Sr(Ag_{1-x}Li_x)_2Se_2$. a) PXRD patterns at $x=0.15$ (top) and $x=0.4$ (middle). A simulated pattern for $x=0.4$ is shown at the bottom to serve as tick marks for reflections whereas their intensities are different due to preferred orientation from the experimental data. b) Unit cell volume as a function of x and c) dependence of x with reaction temperature (T) and r(LiOH).

cycles was also observed in $Sr(Ag_{1-x}Li_x)_2Se_2$ with $x=0.38$ (sample 7 in Table 1), as shown in Figures S2c and d for cycles 1, showing an endothermic event at around 620 °C, and 2–3, respectively. In addition, post-DTA PXRD analysis for both $x=0$ and 0.38 revealed major phases of SrSe and Ag_2Se (Figures S3), suggesting $Sr(Ag_{1-x}Li_x)_2Se_2$ decomposition around 600 °C. It also appears that Li doping increased the stability of $Sr(Ag_{1-x}Li_x)_2Se_2$ because the complete decomposition temperature increased by 40 °C for $x=0.38$. Hence, this tunable flux with mixed LiOH and LiCl can access new parts of the composition space in a given system and form kinetically stable chalcogenides at low temperatures.

We attempted to grow larger crystals of $Sr(Ag_{1-x}Li_x)_2Se_2$ at a very slow cooling rate. In the reaction cool-down from 600 °C with [OH] = 0.80 at a rate of −1 °C/h, we obtained yellow crystals that were lighter in color than $Sr(Ag_{1-x}Li_x)_2Se_2$. The compound was identified as $[Sr_3Se_2][(Ag_{1-x}Li_x)_2Se_2]$ with $x=0.275(4)$, crystallizing in the R-3m space group with $a=4.4111(11)$ and $c=43.211(17)$ Å and consisting of $CaAl_2Si_2$-type $[(Ag_{1-x}Li_x)_2Se_2]$ and rocksalt-type $[Sr_3Se_2]$ layers (Table S9), a unique structure.[16] We are unaware of another intergrowth compound of this type. In addition, it should be possible to further stabilize a homologous series of $[Sr_nSe_{n-1}][(Ag_{1-x}Li_x)_2Se_2]$ with similar structural motifs. The crystallization of other members may be dependent on the synthetic conditions such as temperature and r(LiOH), as we observed the formation of $[Sr_2MnO_2][Cu_{2n(1-x)}S_{n+1}]$ ($n=1$–4) with n as a function of temperature.[18] The slow cooling of the reaction medium enabled the subsequent reaction of $Sr(Ag_{1-x}Li_x)_2Se_2$ with excess Se^{2-} ions inserted in the interlayer space, forming a thin SrSe slab according to the following equation:

$$Sr(Ag_{1-x}Li_x)_2Se_2 + 2Se^{2-} + 2Sr^{2+} \rightarrow [Sr_3Se_2][(Ag_{1-x}Li_x)_2Se_2] \quad (2)$$

Although Li is known to alloy with Ag or Cu in tetrahedral sites of the structure, the Li/Ag alloying usually requires using stoichiometric precursors to target the desired ratios[19] or post-synthetic ion-exchange of a template.[20] LiOH/LiCl fluxes offer precise and facile control of Li substitution by directly correlating the synthetic parameters with x as shown in Figure 1c. For example, at 500 °C the value of x exhibits a linear relationship with r(LiOH) (Figure 1c), which can be used to extrapolate the targeted x as a function of r(LiOH). We attribute this to the tunable solubility of the LiOH/LiCl fluxes, in which increasing LiOH increases the solubility. This Li substitution process for ternary $A_xM_yQ_z$ (A = alkali metal; M = transition metal; Q = S, Se, or Te) is described by the following equation:

$$A_xM_yQ_z\ (s) + \delta Li^+\ (sol) \leftrightarrow A_xM_{y-\delta}Li_\delta Q_z\ (s) + \delta M^+(sol) \quad (3)$$

The internal energy change for replacing each M with Li from the solution is $\Delta\varepsilon = \varepsilon_{Li} - \varepsilon_M + \varepsilon_{M(sol)} - \varepsilon_{Li(sol)}$, where ε_{Li} and ε_M are the internal energies of the M site of the ternary when occupied with one M and Li, respectively. The state signs "(s)" and "(sol)" indicate solid-state and solution states, respectively. Hence, for n number of Li atoms with N of M in the unsubstituted lattice, we can obtain the change in entropy as $S_c/k_B = \ln[N!/(N-n)!/n!] \approx N\ln(N) - N - n\ln(n) - (N-n)\ln(N-n) + (N-n) = N\ln(N) - n\ln(n) - (N-n)\ln(N-n)$, where Sterling's approximation for large numbers was used. Therefore, the following is true for the equilibrium state:

$$\partial\Delta A_d/\partial n = \partial(n\Delta\varepsilon - TS_c)/\partial n = \Delta\varepsilon - k_B T\ln[(N-n)/n] = 0 \quad (4)$$

Thus, $\ln[N/n-1] = \Delta\varepsilon/k_B T$ when Equation (2) is at equilibrium, consistent with our observation that a lower $\Delta\varepsilon$ (or higher solubility) or higher T lead to a larger Li substitution. This explains the generic approach that uses solubility to precisely target the substitution of Li (or other interchangeable elements).

The ability to replace Ag with Li has valuable implications. The strong covalent bonding associated with the Ag–Se interactions is graduate replaced with more ionic

bonding of Li–Se interactions. This lowers the p-orbital energies of Se which dominate the top of the valence band resulting in gradual widening of the band gap without altering the structure type (discussed later in detail). If the degree of Li substitution for Ag can be controlled, precise band gap tunability and thus desirable optoelectronic properties can be achieved.

$SrAg_2Se_2$ crystallizes in a $CaAl_2Si_2$-type structure (*P*-3*m*), in which two-dimensional $[Ag_2Se_2]^{2-}$ layers are interleaved by Sr^{2+} cations (Figures 2a and b). Each $[Ag_2Se_2]^{2-}$ consists of two oppositely stacked layers of AgSe formed by corner-sharing tetrahedra with triangular faces parallel to the *ab* plane, as illustrated in Figure 2c. The local coordination of the edge-sharing $AgSe_4$ tetrahedra opposite each other along the *c*-axis is illustrated in Figure 2d. The lattice parameters, *a* and *c*, and the unit cell volume decrease linearly with increasing *x* (Table 1 and Figure 1b), following Vegard's law of alloying.[21] Our elemental analysis using energy dispersive X-ray spectroscopy (EDS) for $x=0$ and 0.38, shown in Figure S4 and S5, respectively, corroborates the single crystal data. In addition, our Pawley fit showed larger cell volume for $x=0$ (119.41 Å^3, Figure S6) than that of $x=0.38$ (119.41 Å^3, Figure S7). We note that due to the small change in cell volume by Li substitution (≈2 % from $x=0.077$ to 0.438), the single crystal diffraction data, especially those obtained using high-resolution and high-flux synchrotron, are much more reliable than the powder diffraction data. The behavior can be attributed to Li^+ being smaller than Ag^+.[22] For example, the tetrahedral Ag–Se and Li–Se bond lengths are approximately 2.771(1) Å[23] and 2.6002 Å[24] in $Ba_2Ag_2Se_2(Se_2)$ and Li_2Se, respectively. In comparison, the average bond lengths between the AgL^{-1}i and Se sites for $Sr(Ag_{1-x}Li_x)_2Se_2$ were 2.6937(9) Å and 2.7401(6) Å for $x=0.438(6)$ and 0.077(6), respectively. The Ag–Se bond length for $SrAg_2Se_2$ was 2.7329(4) Å at 100 K. Although the Ag–Se bond lengths were the same within the error for each $Sr(Ag_{1-x}Li_x)_2Se_2$, the tetrahedral angles were different, with θ_1 smaller than θ_2 (Figure 2d). In addition, the difference between the two tetrahedral angles decreased with an increased *x*. For $x=0.438(6)$, θ_2 and θ_1 were 109.85(4) and 109.09(4)°, respectively, whereas for $x=0.077(6)$, θ_2 and θ_1 were 111.16(3) and 107.73(3)°, respectively. Thus, with increasing *x*, the $AgSe_4$ in $Sr(Ag_{1-x}Li_x)_2Se_2$ evolves toward an ideal tetrahedron.

The heterolayered $[Sr_3Se_2][(Ag_{1-x}Li_x)_2Se_2]$ in the *R*-3*m* space group (Figures 2e and f) consists of $CaAl_2Si_2$-type $[(Ag_{1-x}Li_x)_2Se_2]$ layers, similar to those in $Sr(Ag_{1-x}Li_x)_2Se_2$. Instead of cation separators such as Sr^{2+}, the $[(Ag_{1-x}Li_x)_2Se_2]$ layers are separated by $[Sr_3Se_2]$ consisting of three octahedral thick slabs of rocksalt-type SrSe, as shown in Figures 2e and f. The slabs are slices of the NaCl lattice with cuts perpendicular to the [111] direction. For the sample prepared at $T=600$ °C with [OH] = 0.80, the corresponding *x* was 0.275(4) with $a=4.4111(11)$ Å and $c=43.211(17)$ Å. The Ag–Se bond length was 2.7171(7) Å, similar to the distance of 2.7165(4) Å for $x=0.255(4)$ in $Sr(Ag_{1-x}Li_x)_2Se_2$. Because each $AgSe_4$ tetrahedron in the Ag layers shares the same triangular face with its neighboring $SrSe_6$ octahedra in the Sr layers, the lattice match between these building blocks is crucial for the stability of their intergrown structures. In $[Sr_3Se_2][(Ag_{1-x}Li_x)_2Se_2]$, the Se–Se distance for the shared triangles is 4.4111(12) Å (the same as the lattice constant *a*), very similar to the Se–Se distance, 4.4153(9) Å, in the triangular faces of $SrSe_6$ octahedra in binary rocksalt-type SrSe.[25] It is likely that the lattice compatibility between SrSe and $Sr(Ag_{1-x}Li_x)_2Se_2$ allowed the formation of $[Sr_3Se_2]$-$[(Ag_{1-x}Li_x)_2Se_2]$ by kinetically stacking the respective building blocks.

To understand the nature of the electronic properties of $Sr(Ag_{1-x}Li_x)_2Se_2$, we performed electronic structure calculations using DFT for $[Sr_3Se_2][Ag_2Se_2]$ and $Sr(Ag_{1-x}Li_x)_2Se_2$ with $x=0$, 0.5, and 1 (Figure 3). All three compositions of $Sr(Ag_{1-x}Li_x)_2Se_2$ exhibited direct band gap at the **Γ**-point with band gap energies (E_g) of 0.55, 1.17, and 2.93 eV for $x=$ 0, 0.5 and 1, respectively (Figures 3a–c), suggesting increased Li substitution at the Ag site increased E_g. This can be attributed to the interactions between Ag-4d and Se-4p that raise the valence band maximum (VBM) toward the conduction band, as shown in the −2 to 0 eV region in the density of state (DOS) plots shown in Figures 3a and b. In comparison, Li-2s was buried too deep in the energy level and mainly left the Se-4p states in the VBM for $x=1$ (Figure 3c). When Ag is completely substituted by Li, the VBM decreases to being composed of the Se-4p bands (Figure 3c). The energy level at about $E=-2.2$ eV in the DOS plot in Figure 3a is now equivalent to the new Fermi level of that of Figure 3c, increasing E_g from 0.55 to 2.93 eV.

The heterolayered $[Sr_3Se_2][Ag_2Se_2]$ also show a direct band gap at the **Γ**-point with $E_g=1.27$ eV (Figure 3d), which is 0.72 eV larger than $SrAg_2Se_2$ without any Li substitution. Its VBM consists primarily of Ag-4d and Se-4p states (DOS in Figure 3d), similar to that of $SrAg_2Se_2$. However, the thick $[Sr_3Se_2]$ slabs and open a wider band gap, consistent with SrSe (2.19 eV)[26] having considerably larger E_g than $SrAg_2Se_2$ (0.55 eV). Hence, it is likely that thicker SrSe layers lead to a larger E_g, similar to the effect of Li substitution on the Ag site. Because there are three SrSe slabs for every Ag_2Se slab, $[Sr_3Se_2][Ag_2Se_2]$ can be considered as a 3-layer ultrathin film of NaCl-type SrSe cut along the diagonal from the bulk. Note that NaCl-type SrSe is an indirect band gap semiconductor (**Γ** to **X**).[26] The change from cubic symmetry to hexagonal and bulk cubic SrSe to highly directional 3-layer slabs leads to the emergence of a direct band gap in $[Sr_3Se_2][Ag_2Se_2]$.

The UV/Vis measurements suggest that $Sr(Ag_{1-x}Li_x)_2Se_2$ are semiconductors whose E_g values increase with increasing values of *x*. The corresponding values of E_g for $x=0$, 0.15, and 0.38 were 1.59, 1.80 and 1.95 eV, respectively, as shown in Figure 4a. The results are consistent with the colors of the crystals, which are black with a metallic luster, red, and orange for $x=0$, 0.15 and 0.38, respectively (Figure 4a insets). However, we noticed that the powders of the ground crystals turned darker after extensive grinding in air and the measurements incorrectly showed smaller than expected band gaps, suggesting sensitivity to air or moisture. Exposure to moisture can lead to surface degradation of materials with smaller gaps, such as Se. It should be noted that this effect is likely confined to the surface, as the

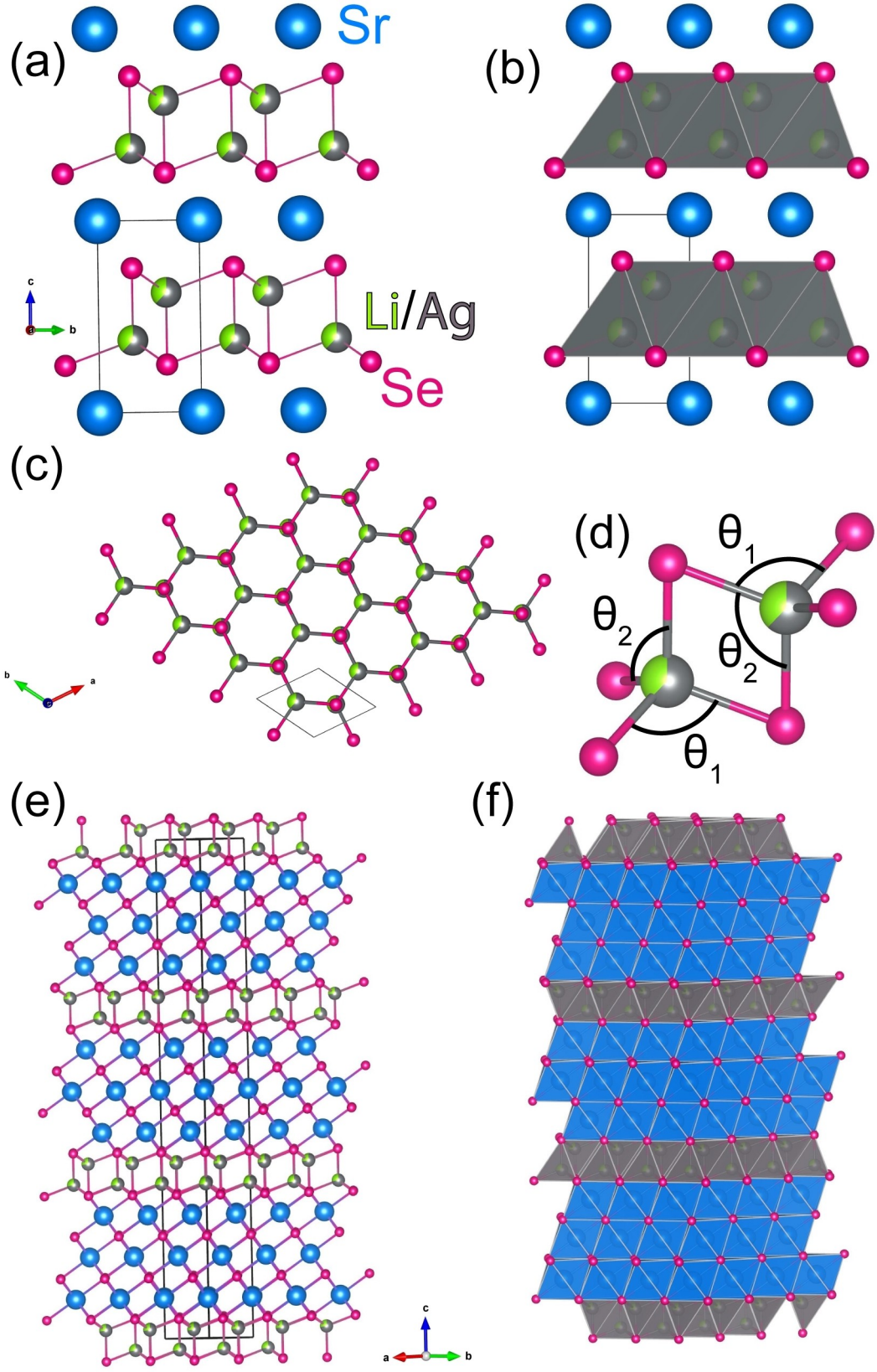

Figure 2. Structures of $Sr(Ag_{1-x}Li_x)_2Se_2$, crystallizing in a $CaAl_2Si_2$–type structure (*P*-3*m* space group with $a = 4.4096(2)$ and $c = 7.1966(4)$ Å), along the *a*-axis in a) ball-stick and b) polyhedral representations and along c) *c*-axis with Sr atom hidden for clarity. d) Edge-sharing $AgSe_4$ tetrahedra in $Sr(Ag_{1-x}Li_x)_2Se_2$ and structures of $[Sr_3Se_2][(Ag_{1-x}Li_x)_2Se_2]$, crystallizing in the *R*-3*m* space group with $a = 4.4111(11)$ and $c = 43.211(17)$ Å, along the [110] axis in e) ball-stick and f) polyhedral representations. The Sr, Ag, Li and Se atoms are shown in blue, gray, green and crimson, respectively.

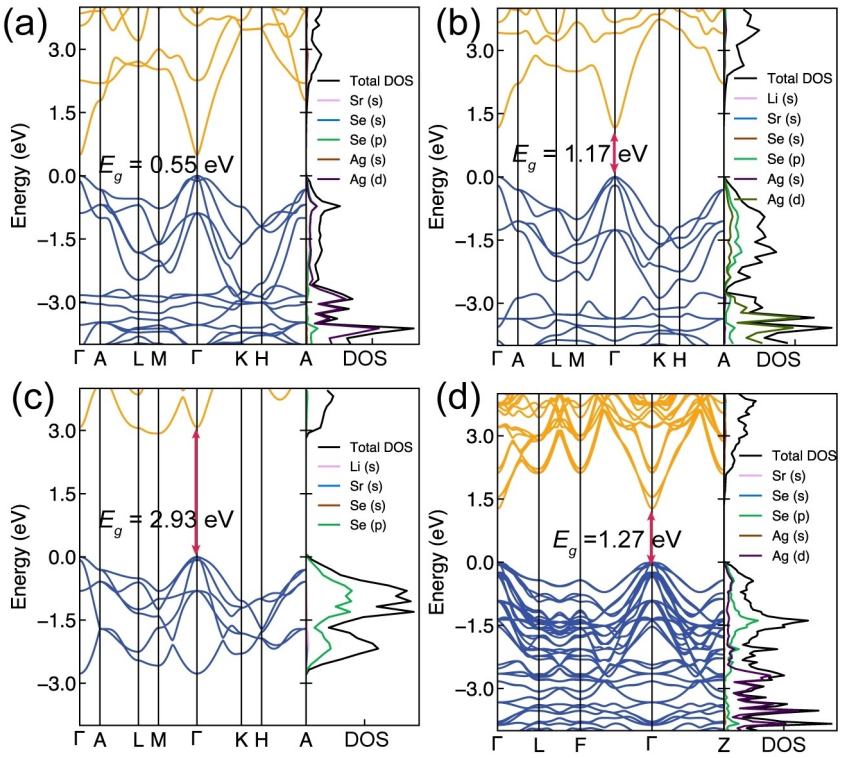

Figure 3. Band structures and the corresponding density of state (DOS) plots of $Sr(Ag_{1-x}Li_x)_2Se_2$ for a) $x=0$, b) $x=0.5$, and c) $x=1$. d) Density of states of $[Sr_3Se_2][Ag_2Se_2]$. The calculated band gap energies (E_g) for a), b), c) and d) are 0.55, 1.17, 2.93 and 1.27 eV, respectively. A 2×2×1 superstructure was constructed for the calculations at $x=0.5$ ($SrAgLiSe_2$).

unground samples in the form of 50–300 μm crystals remained unchanged after being washed with water and stored in air for two years. Nonetheless, this increase in the band gap after Li substitution originates from the decreased covalency in the structure as Ag–Se bonds are replaced with more ionic Li–Se bonds and is consistent with our DFT calculations and other semiconducting Ag/Cu-containing chalcogenides, such as Ag_2ZnSnS_4 or Cu_2ZnSnS_4.[19] Hence, the band gap of $Sr(Ag_{1-x}Li_x)_2Se_2$ is tunable by adjusting the synthetic parameters.

$Sr(Ag_{1-x}Li_x)_2Se_2$ also showed photoluminescence (PL) with broad emission under a 405 nm laser, as shown in Figure 4b. The intensities of the emission spectra increased significantly with an increased x. No emission was observed for $x=0$. For $x=0.15$, the emission was identified but was fairly weak with a low signal/noise ratio. However, for $x=0.38$, a strong emission spectrum was observed (Figure 4b) with intensities over an order of magnitude stronger than those for $x=0.15$. The emission spectrum for $x=0.38$ appeared at around 600 nm (equivalent to 2.06 eV), which corresponds to orange, consistent with the color of the crystal (Figure 4a inset for $x=0.38$). The time-resolved PL for $x=0.38$ after removal of high-frequency instrument noise using Fourier filter[27] is shown in Figure 4c. Its PL decay time (τ) was estimated to be approximately 8 ns.

Conclusion

Mixed hydroxide/halide fluxes offer adjustable solubility of reactants and intermediates, enabling easy synthesis of new direct band gap semiconductors of the $Sr(Ag_{1-x}Li_x)_2Se_2$ series. Precise control of the x value in this series is achievable through temperature and LiOH fraction in the flux, improving synthesis efficiency. This allows for direct correlation between material properties and synthesis parameters. The flux's high solubility also enables co-precipitation of different building blocks, making it suitable for creating heterolayered structures. By adjusting only a few key parameters such as temperature or acidity, this tunable flux approach is a powerful tool for phase selection, potentially speeding up the discovery and design of new materials.

Supporting Information

Supporting Information is available free at. Additional powder and single-crystal X-ray diffraction and differential thermal analysis. Additional crystallographic information (CIF): CSD deposit numbers: 2192113 (Table S1), 2192145 (Table S2), 2192153 (Table S8), 2192154 (Table S6), 2192155 (Table S7), 2192156 (Table S3), 2192157 (Table S5), 2192158 (Table S4) and 2192176 (Table S9) contain all the crystallographic data shown from Table S1–S9.

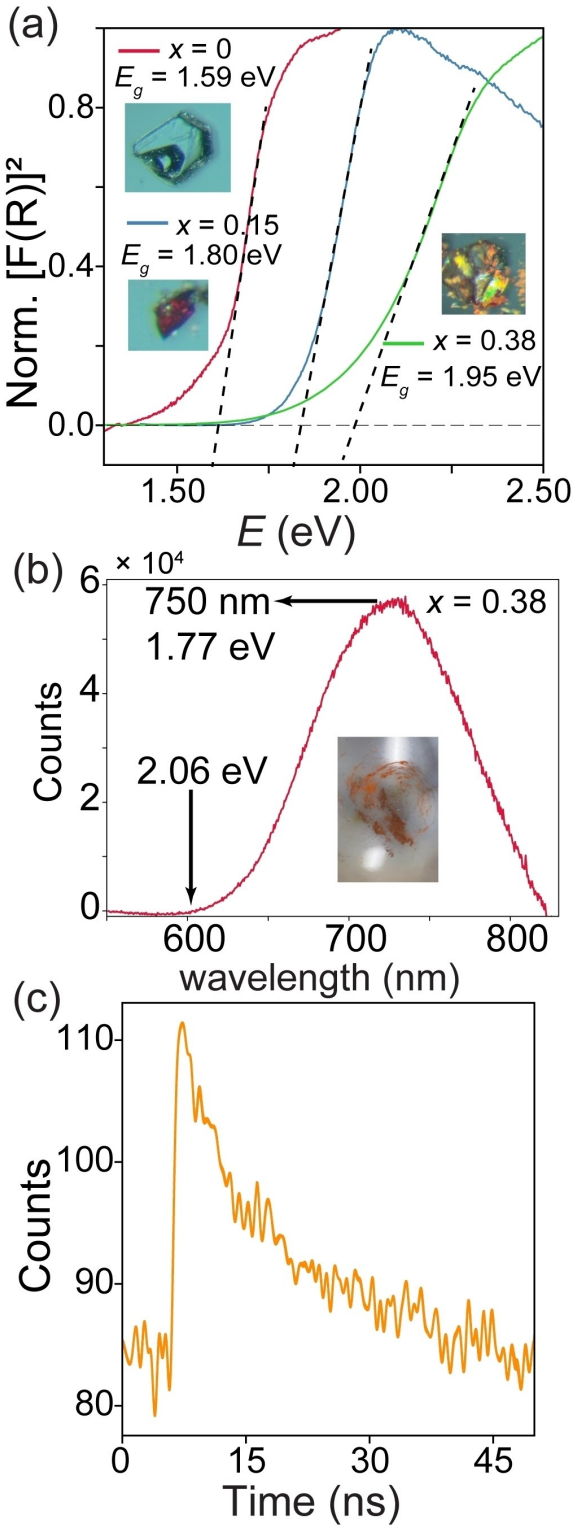

Figure 4. Optical properties of the samples. a) UV/Vis absorbance spectra (derived from diffuse reflectance measurements) of Sr-$(Ag_{1-x}Li_x)_2Se_2$ for $x=0.1$, 0.15 and 0.38. The anomalous peaks shown below 1 eV were because of instrumental artifacts. b) Photoluminescence (PL) spectrum of the Sr$(Ag_{1-x}Li_x)_2Se_2$ sample with $x=0.38$. c) Time-resolved PL curve after noise removal using Fourier filter of the sample in (b) at 750 nm. The band gap energies (E_g) for (a), (b), and (c) are 1.59, 1.80, and 1.95 eV, respectively. The insets in (a) shows the color of the crystals for each sample with different *x*.

Acknowledgements

This work was supported by the U.S. Department of Energy, Office of Science, Basic Energy Sciences, Materials Sciences, and Engineering Division. The use of the Advanced Photon Source (APS) and Center for Nanoscale Materials (CNM) at Argonne National Laboratory, an Office of Science User Facilities, was supported by the U.S. Department of Energy, Office of Science under Contract No. DE-AC02-06CH11357. NSF's ChemMatCARS Sector 15 at APS was supported by the Division of Chemistry (CHE) and Materials Research (DMR), National Science Foundation, under grant number NSF/CHE-1834750. The authors acknowledge the University of Maryland supercomputing resources made available for conducting the band calculations reported in this paper.

Conflict of Interest

The authors declare no competing financial interest.

Data Availability Statement

The data that support the findings of this study are available in the Supporting Information of this article.

Keywords: 2D Materials · Chalcogenides · Flux Synthesis · Semiconductor

[1] a) A. Stein, S. W. Keller, T. E. Mallouk, *Science* **1993**, *259*, 1558–1564; b) M. G. Kanatzidis, *Chem. Mater.* **1990**, *2*, 353–363; c) M. G. Kanatzidis, *Inorg. Chem.* **2017**, *56*, 3158–3173; d) W. M. Chance, D. E. Bugaris, A. S. Sefat, H.-C. zur Loye, *Inorg. Chem.* **2013**, *52*, 11723–11733; e) D. E. Bugaris, H. C. zur Loye, *Angew. Chem. Int. Ed.* **2012**, *51*, 3780–3811; *Angew. Chem.* **2012**, *124*, 3844–3876; f) J. Y. Chan, S. Dehnen, *Inorg. Chem.* **2020**, *59*, 17823–17825; g) D. C. Schmitt, B. L. Drake, G. T. McCandless, J. Y. Chan, *Acc. Chem. Res.* **2015**, *48*, 612–618; h) S. E. Latturner, *Acc. Chem. Res.* **2018**, *51*, 40–48; i) P. C. Canfield, Z. Fisk, *Philos. Mag. B* **1992**, *65*, 1117–1123; j) P. C. Canfield, *Rep. Prog. Phys.* **2020**, *83*, 016501; k) J. Wang, P. Yox, K. Kovnir, *Front. Chem.* **2020**, *8*, 186.

[2] S. J. Mugavero III, W. R. Gemmill, I. P. Roof, H.-C. zur Loye, *J. Solid State Chem.* **2009**, *182*, 1950–1963.

[3] a) H. Flood, T. Förland, *Acta Chem. Scand.* **1947**, *1*, 592–606; b) H. Lux, R. Kuhn, T. Niedermaier, *Z. Anorg. Allg. Chem.* **1959**, *298*, 285–301.

[4] a) D. E. Bugaris, M. D. Smith, H.-C. zur Loye, *Inorg. Chem.* **2013**, *52*, 3836–3844; b) R. Albrecht, F. Graßme, T. Doert, M. Ruck, *Z. Naturforsch. B* **2020**, *75*, 951–957.

[5] R. Albrecht, M. Ruck, *Angew. Chem. Int. Ed.* **2021**, *60*, 22570–22577; *Angew. Chem.* **2021**, *133*, 22744–22752.

[6] X. Zhou, D. J. Mandia, H. Park, M. Balasubramanian, L. Yu, J. Wen, A. Yakovenko, D. Y. Chung, M. G. Kanatzidis, *J. Am. Chem. Soc.* **2021**, *143*, 13646–13654.

[7] P. Chiotti, R. Markuszewski, *J. Chem. Eng. Data* **1985**, *30*, 197–201.

[8] X. Zhou, V. S. C. Kolluru, W. Xu, L. Wang, T. Chang, Y.-S. Chen, L. Yu, J. Wen, M. K. Y. Chan, D. Y. Chung, M. G. Kanatzidis, *Nature* **2022**, *612*, 72–77.
[9] a) M. Dalmases, M. Ibáñez, P. Torruella, V. Fernàndez-Altable, L. López-Conesa, D. Cadavid, L. Piveteau, M. Nachtegaal, J. Llorca, M. L. Ruiz-González, S. Estradé, F. Peiró, M. V. Kovalenko, A. Cabot, A. Figuerola, *Chem. Mater.* **2016**, *28*, 7017–7028; b) K. Pal, Y. Xia, J. Shen, J. He, Y. Luo, M. G. Kanatzidis, C. Wolverton, *npj Comput. Mater.* **2021**, *7*, 82; c) J. M. Hodges, Y. Xia, C. D. Malliakas, G. C. B. Alexander, M. K. Y. Chan, M. G. Kanatzidis, *Chem. Mater.* **2018**, *30*, 7245–7254; d) J. He, Y. Xia, W. Lin, K. Pal, Y. Zhu, M. G. Kanatzidis, C. Wolverton, *Adv. Funct. Mater.* **2022**, *32*, 2108532; e) C. Zhang, J. He, R. McClain, H. Xie, S. Cai, L. N. Walters, J. Shen, F. Ding, X. Zhou, C. D. Malliakas, J. M. Rondinelli, M. G. Kanatzidis, C. Wolverton, V. P. Dravid, K. R. Poeppelmeier, *J. Am. Chem. Soc.* **2022**, *144*, 2569–2579.
[10] A. J. E. Rettie, J. Ding, X. Zhou, M. J. Johnson, C. D. Malliakas, N. C. Osti, D. Y. Chung, R. Osborn, O. Delaire, S. Rosenkranz, M. G. Kanatzidis, *Nat. Mater.* **2021**, *20*, 1683–1688.
[11] V. A. Starodub, *Russ. Chem. Rev.* **1999**, *68*, 801–820.
[12] W. Bronger, B. Lenders, J. Huster, *Z. Anorg. Allg. Chem.* **1997**, *623*, 1357–1360.
[13] H. Li, S.-J. Hwu, *Angew. Chem. Int. Ed.* **1999**, *38*, 3067–3070; *Angew. Chem.* **1999**, *111*, 3253–3256.
[14] C. E. Check, C. Zheng, J. Zhang, B. Dabrowski, *J. Solid State Chem.* **1999**, *144*, 409–415.
[15] D. G. Chica, Y. He, K. M. McCall, D. Y. Chung, R. O. Pak, G. Trimarchi, Z. Liu, P. M. De Lurgio, B. W. Wessels, M. G. Kanatzidis, *Nature* **2020**, *577*, 346–349.
[16] Deposition Numbers 2192113, 2192145, 2192153, 2192154, 2192155, 2192156, 2192157, 2192158, and 2192176 contain the supplementary crystallographic data for this paper. These data are provided free of charge by the joint Cambridge Crystallographic Data Centre and Fachinformationszentrum Karlsruhe Access Structures service.
[17] M. Pourbaix, *Atlas of Electrochemical Equilibria in Aqueous Solutions*, National Association of Corrosion Engineers, Houston, **1974**.
[18] X. Zhou, C. D. Malliakas, A. A. Yakovenko, B. Wilfong, S. G. Wang, Y.-S. Chen, L. Yu, J. Wen, M. Balasubramanian, H.-H. Wang, D. Y. Chung, M. G. Kanatzidis, *Nat. Synth.* **2022**, *1*, 729–737.
[19] a) W. Zhou, Q. Zhang, W.-D. Yao, H. Xue, S.-P. Guo, *Inorg. Chem.* **2021**, *60*, 12536–12544; b) A. Lafond, C. Guillot-Deudon, J. Vidal, M. Paris, C. La, S. Jobic, *Inorg. Chem.* **2017**, *56*, 2712–2721.
[20] a) S. Indris, J. Cabana, O. J. Rutt, S. J. Clarke, C. P. Grey, *J. Am. Chem. Soc.* **2006**, *128*, 13354–13355; b) I. Suzuki, Y. Mizuno, T. Omata, *Inorg. Chem.* **2019**, *58*, 4262–4267.
[21] A. R. Denton, N. W. Ashcroft, *Phys. Rev. A* **1991**, *43*, 3161.
[22] R. D. Shannon, *Acta Crystallogr. Sect. A* **1976**, *32*, 751–767.
[23] S. Jana, M. Ishtiyak, A. Mesbah, S. Lebègue, J. Prakash, C. D. Malliakas, J. A. Ibers, *Inorg. Chem.* **2019**, *58*, 7837–7844.
[24] E. Zintl, A. Harder, B. Dauth, *Z. Elektrochem. Angew. Phys. Chem.* **1934**, *40*, 588–593.
[25] T. Petzel, J. Kohle, *Z. Anorg. Allg. Chem.* **1977**, *437*, 193–196.
[26] R. Khenata, H. Baltache, M. Rérat, M. Driz, M. Sahnoun, B. Bouhafs, B. Abbar, *Physica B: Condensed Matter* **2003**, *339*, 208–215.
[27] V. J. Barclay, R. F. Bonner, I. P. Hamilton, *Anal. Chem.* **1997**, *69*, 78–90.

Manuscript received: January 23, 2023
Accepted manuscript online: January 27, 2023
Version of record online: February 23, 2023